Electronic Supplementary Material (ESI) for Chemical Communications.

Contents:

1. Materials

Bis(diphenylphosphino)methane (dppm) was purchased from Tokyo Chemical Industry Co., Ltd. Copper(I) chloride (CuCl), dichloromethane (CH_2Cl_2), methanol (MeOH) and acetonitrile (MeCN) were purchased from Nacalai Tesque, Inc (Kyoto, Japan). *n*-Hexane and diethyl ether (Et_2O) were purchased from FUJIFILM Wako Pure Chemical Industry, Ltd (Osaka, Japan). Bis(diphenylarsino)methane (dpam),[1] Au_2Cl_2(dpam),[2] and Au_2Cl_2(dppm)[3] were prepared according to the literature procedures.

2. Measurement

^{1}H (400 MHz) and ^{13}C (100 MHz) nuclear magnetic resonance (NMR) spectra were recorded on a Bruker AVANCE III 400 NMR spectrometer. High resolution mass spectra (HRMS) were obtained on a JEOL JMS-700 spectrometer. Emission and excitation spectra were obtained on an FP-8500 (JASCO) spectrometer and the absolute PL quantum yields (Φ) were determined by using a JASCO ILFC-847S; the quantum yield of quinine sulfate as reference was 0.52, which is in agreement with the literature value.[4] Emission lifetimes were measured by using a Quantaurus-Tau (Hamamatsu Photonics, Shizuoka, Japan) instrument. Powder X-ray diffractometry (PXRD) studies were performed on a Rigaku Smartlab X-ray diffractometer with CuK_α radiation (λ = 1.5406 Å) in the $2\theta/\theta$ mode and a Rigaku MiniFlex600 X-ray diffractometer using X-rays from a 600 W X-ray tubes (CuKα, λ = 1.54 Å) and a D/teX Ultra2 semiconductor detector at room temperature. The 2θ scan data were collected at 0.01° intervals and the scan speed was 10° (2θ) / min.

3. X-ray crystallographic data for single crystalline products

The single crystal was mounted on a glass fiber. Intensity data were collected at room temperature on a Rigaku XtaLAB mini with graphite monochromated Mo Kα radiation. Readout was performed in the 0.073 mm pixel mode. Data were processed using the CrysAlisPro.[5] An analytical numeric absorption correction[6] was applied. The data were corrected for Lorentz and polarization effects. The structure was solved by ShelXT (Intrinsic Phasing)[7] and expanded using Fourier techniques. Non-hydrogen atoms were refined anisotropically. Hydrogen atoms were refined using the riding model. The final cycle of full-matrix least-squares refinement on F^2 was based on observed reflections and variable parameters. All calculations were performed using the $Olex_2$[8] crystallographic software package except for refinement, which was performed using

SHELXL2016.[9]

4. Synthesis

$[Au_2(dpam)_2]$-$[CuCl_2]_2$ (1): To a CH_2Cl_2 solution (10 mL) of dpam (25 mg, 54 μmol) and Au_2Cl_2(dpam) (50 mg, 54 μmol) was added a MeCN (10 mL) solution of CuCl (13 mg, 0.13 mmol) and stirring for 1 h. After removing the volatiles *in vacuo*, the residue was dissolved in CH_2Cl_2 and gently added *n*-hexane to obtain **1** as pale green crystals (90 mg, quant.). The crystals were insoluble in organic solvents. Elemental analysis: calculated for $C_{50}H_{44}As_4Au_2Cl_4Cu_2$ (containing 5 w% of CH_2Cl_2) C 36.20; H 2.74, found: C 35.88; H 2.82. *α*-**1**: recrystallization from CH_2Cl_2/*n*-hexane, *β*-**1**: recrystallization from CH_2Cl_2/MeCN/Et_2O (CH_2Cl_2/MeCN/Et_2O = 2/1/3), *γ*-**1**: recrystallization from CH_2Cl_2/MeOH.

$[Au_2(dppm)_2]$-$[CuCl_2]_2$ (2): To a CH_2Cl_2 solution (10 mL) of dppm (23 mg, 59 μmol) and Au_2Cl_2(dppm) (50 mg, 59 μmol) was added a MeCN (10 mL) solution of CuCl (14 mg, 0.14 mmol) and stirring for 1 h. After removing the volatiles *in vacuo*, the residue was dissolved in CH_2Cl_2 and gently added *n*-hexane. The *α* type crystals were collected by filtration to obtain **2** as pale green crystals (82 mg, 97%). Elemental analysis: calculated for $C_{50}H_{44}P_4Au_2Cl_4Cu_2$ (containing 7 w% of CH_2Cl_2) C 40.00; H 3.05, found: C 39.79; H 2.94. The crystals were insoluble in organic solvents. *α*-**2**: recrystallization from CH_2Cl_2/*n*-hexane, *β*-**2**: recrystallization from CH_2Cl_2/MeCN/Et_2O (CH_2Cl_2/MeCN/Et_2O = 2/1/3), *γ*-**2**: recrystallization from CH_2Cl_2/MeOH.

5. Crystal data

Table S1. Crystallographic data of α-**1**, β-**1**, and γ-**1**.

Crystal data	α-**1**	β-**1**	γ-**1**
Empirical formula	$C_{51}H_{46}As_4Au_2Cl_6Cu_2$	$C_{51.27}H_{46.55}As_4Au_2Cl_{6.55}Cu_2$	$C_{50}H_{44}As_4Au_2Cl_4Cu_2$
Formula weight	1777.19	1715.50	1607.34
Crystal Dimension, mm^3	0.37 × 0.11 × 0.09	0.32 × 0.12 × 0.11	0.2 × 0.2 × 0.2
Crystal system	triclinic	monoclinic	monoclinic
Space group	*P*-1	*C*2/*c*	*C*2/*c*
a, Å	9.8863(6)	24.4022(13)	22.036(4)
b, Å	12.8738(9)	9.8331(4)	15.6209(18)
c, Å	13.3885(8)	26.3594(15)	16.343(3)
α, deg	62.963(6)	90	90
β, deg	69.397(6)	116.103(7)	114.380(6)
γ, deg	81.811(5)	90	90
Volume, $Å^3$	1420.40(18)	5679.8(6)	5124.0(13)
D_{calcd}, g cm^{-3}	2.078	2.006	2.084
Z	1	4	4
F(000)	844.0	3254.00	3040.0
Data collection			
Temperature, °C	-180.0	-180.0	25.0
$2\theta_{max}$, deg	52.74	52.744	54.968
T_{min}/T_{max}	0.905/0.966	0.746/0.838	0.667/1.000
Refinement			
No. of observed data	5801	5807	5856
No. of parameters	307	308	330
R1[a], wR2 [b]	0.0351, 0.0615	0.0318, 0.0556	0.0485, 0.1168
Goodness of fit indicator	0.988	1.031	1.044

[a]$R1 = \Sigma \mid |Fo| - |Fc| \mid / \Sigma|Fo|$, [b]$wR2 = [\Sigma w ((Fo^2 - Fc^2)^2 / \Sigma w (Fo^2)^2]^{1/2}$, $w = [\delta^2(Fo^2)]^{-1}$

CCDC # 2064781 (α-**1**), 2064785 (β-**1**), and 2064782 (γ-**1**)

Table S2. Crystallographic data of α-**2**, β-**2**, and γ-**2**.

Crystal data	α-**2**	β-**2**	γ-**2**
Empirical formula	$C_{52}H_{48}Au_2Cl_8Cu_2P_4$	$C_{51}H_{46}Au_2Cl_6Cu_2P_4$	$C_{100}H_{88}Au_4Cl_8Cu_4P_8$
Formula weight	1601.39	1516.47	2863.08
Crystal Dimension, mm^3	0.37 × 0.08 × 0.07	0.347 × 0.11 × 0.081	0.41 × 0.2 × 0.14
Crystal system	triclinic	monoclinic	triclinic
Space group	*P*-1	C2/c	*P*-1
a, Å	9.9269(3)	24.0857(16)	11.9552(4)
b, Å	12.6985(8)	9.8217(4)	14.8332(4)
c, Å	13.1817(8)	26.0584(19)	14.8676(5)
α, deg	110.431(6)	90	78.576(2)
β, deg	111.146(5)	116.602(9)	78.834(3)
γ, deg	98.196(4)	90	69.834(3)
Volume, $Å^3$	1382.04(14)	5511.9(7)	2403.25(14)
D_{calcd}, g cm^{-3}	1.924	1.827	1.978
Z	1	4	1
F(000)	772.0	2920.0	1376.0
Data collection			
Temperature, °C	-180.0	-180.0	-180.0
$2\theta_{max}$, deg	52.746	52.742	65.46
T_{min}/T_{max}	0.271/0.687	0.404/0.563	0.829/1.000
Refinement			
No. of observed data	5662	5640	15415
No. of parameters	307	307	559
R1[a], wR2 [b]	0.0281, 0.0626	0.0321, 0.0705	0.0374, 0.0587
Goodness of fit indicator	1.025	1.051	0.988

[a]$R1 = \Sigma \mid |Fo| - |Fc| \mid / \Sigma|Fo|$, [b]$wR2 = [\ \Sigma\ w\ ((Fo^2 - Fc^2)^2 / \Sigma\ w\ (Fo^2)^2]^{1/2}$, $w = [\delta^2(Fo^2)]^{-1}$

CCDC # 2064786 (α-**2**), 2064784 (β-**2**), 2064783 (γ-**2**)

Table S4. ORTEP drawing (ellipsoids at 50% probability), selected distances, and angles of α-**1**.

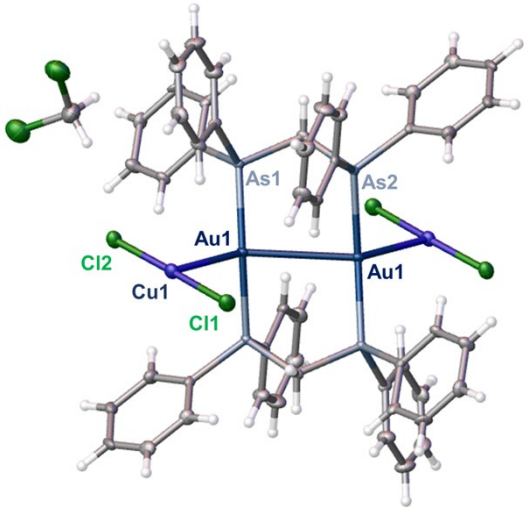

distances (Å)		angles (°)	
Au1–Au1	3.1408(4)	As1–Au1–As2	164.13(2)
Au1–Cu1	2.7491(9)	As1–Au1–Cu1	102.31(2)
Cu1–Cl1	2.112(2)	Cl1–Cu1–Cl2	176.83(8)
Cu1–Cl2	2.111(2)		
Au1–As1	2.4026(6)		
Au1–As2	2.4108(6)		

Table S5. ORTEP drawing (ellipsoids at 50% probability), selected distances, and angles of *β*-**1**.

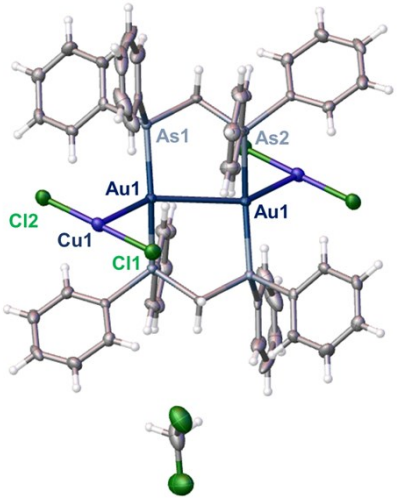

distances (Å)		angles (°)	
Au1–Au1	3.1636(7)	As1–Au1–As2	163.70(3)
Au1–Cu1	2.7868(7)	As1–Au1–Cu1	103.34(2)
Cu1–Cl1	2.116(2)	Cl1–Cu1–Cl2	177.73(8)
Cu1–Cl2	2.103(2)		
Au1–As1	2.3965(6)		
Au1–As2	2.4083(6)		

Table S6. ORTEP drawing (ellipsoids at 50% probability), selected distances, and angles of γ-**1**.

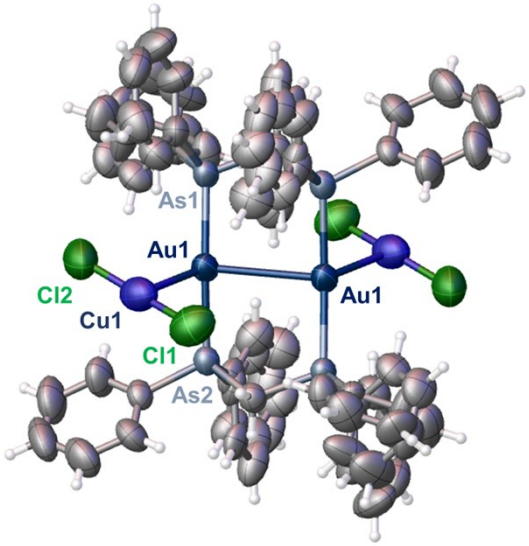

distances (Å)		angles (°)	
Au1–Au1	3.1192(7)	As1–Au1–As2	168.12(3)
Au1–Cu1	2.861(1)	As1–Au1–Cu1	107.54(4)
Cu1–Cl1	2.071(5)	Cl1–Cu1–Cl2	173.7(2)
Cu1–Cl2	2.077(5)		
Au1–As1	2.408(1)		
Au1–As2	2.4067(9)		

Comments for the level-A alerts of CheckCIF of γ-1

Alert level A
PLAT770_ALERT_2_A Suspect C-H Bond in CIF: C21A --H21A . 1.58 Ang.

The crystal was relatively unstable. It was thus difficult to grow single crystals with high quality, though we had tried many times. We also tried the measurements at 93 K, but the crystal was broken during the measurement. However, in this work, we discussed the structures around Au and Cu atoms, which can be assessed by the present data.

Table S7. ORTEP drawing (ellipsoids at 50% probability), selected distances, and angles of α-**2**.

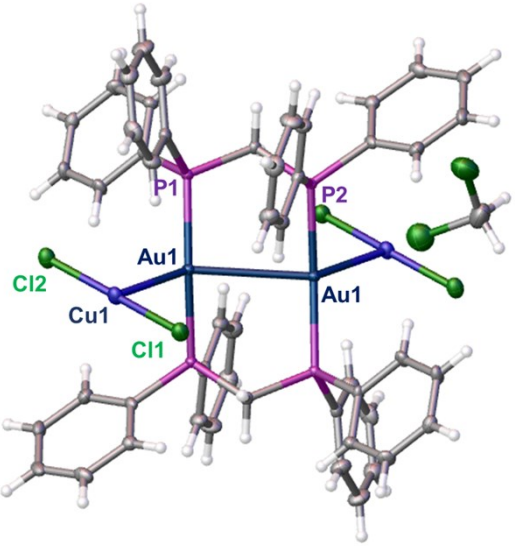

distances (Å)		angles (°)	
Au1–Au1	3.0656(4)	As1–Au1–As2	164.21(5)
Au1–Cu1	2.7705(6)	As1–Au1–Cu1	104.09(3)
Cu1–Cl1	2.117(2)	Cl1–Cu1–Cl2	174.64(6)
Cu1–Cl2	2.117(2)		
Au1–As1	2.316(1)		
Au1–As2	2.325(1)		

Table S8. ORTEP drawing (ellipsoids at 50% probability), selected distances, and angles of *β*-**2**.

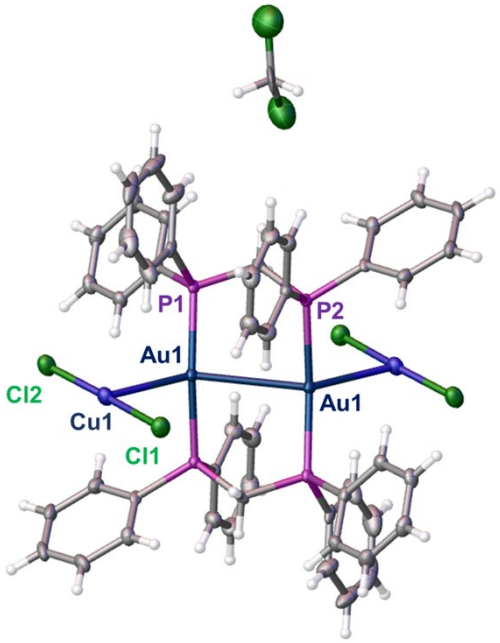

distances (Å)		angles (°)	
P1–Au1	3.0835(7)	P1–Au1–P2	163.61(5)
Au1–Cu1	2.8118(7)	P1–Au1–Cu1	104.60(4)
Cu1–Cl1	2.118(2)	Cl1–Cu1–Cl2	175.45(7)
Cu1–Cl2	2.106(2)		
Au1–P1	2.313(1)		
Au1–P2	2.324(1)		

Table S9. ORTEP drawing (ellipsoids at 50% probability), selected distances, and angles of *γ*-**2**.

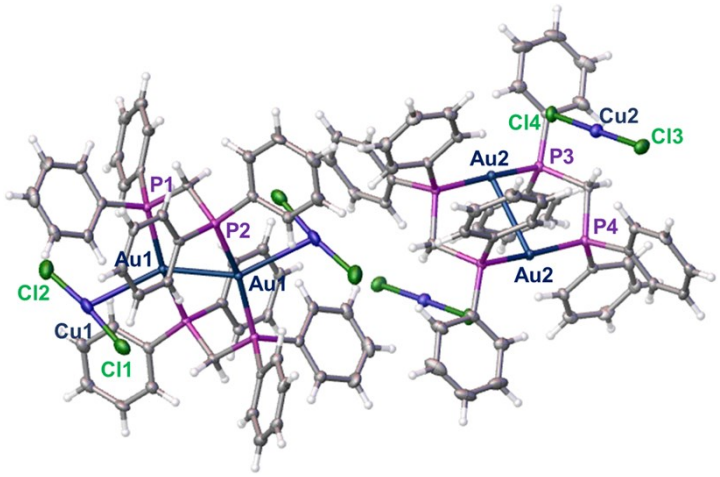

distances (Å)		angles (°)	
Au1–Au1	2.9785(5)	P1–Au1–P2	165.28(4)
Au2–Au2	2.9594(4)	P3–Au2–P4	168.43(4)
Au1–Cu1	2.8465(6)	P1–Au1–Cu1	97.66(3)
Au2–Cu2	4.7413(7)	P3–Au2–Cu2	82.29(3)
Cu1–Cl1	2.122(2)	Cl1–Cu1–Cl2	173.67(7)
Cu1–Cl2	2.118(2)	Cl3–Cu2–Cl4	179.10(6)
Cu2–Cl3	2.086(2)		
Cu2–Cl4	2.090(2)		
Au1–P1	2.308(1)		
Au1–P2	2.325(1)		
Au2–P3	2.325(1)		
Au2–P4	2.309(1)		

6. Powder XRD patterns

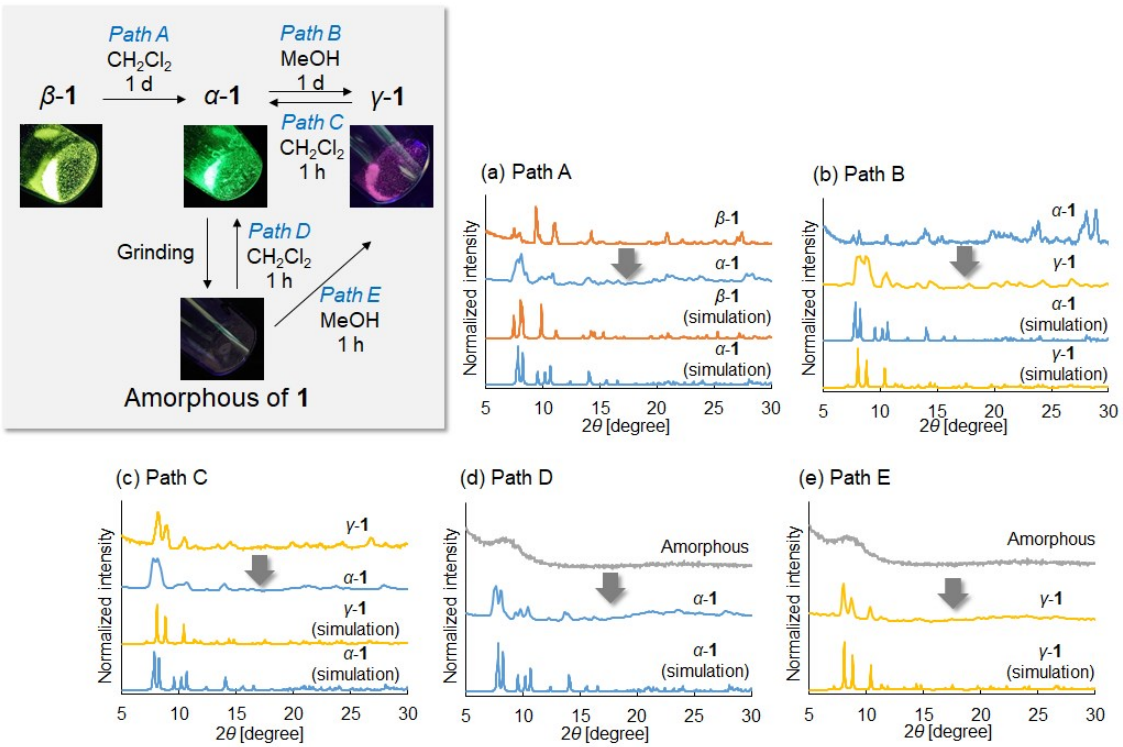

Figure S1. PXRD patterns of **1** for vapor-induced phase transitions.

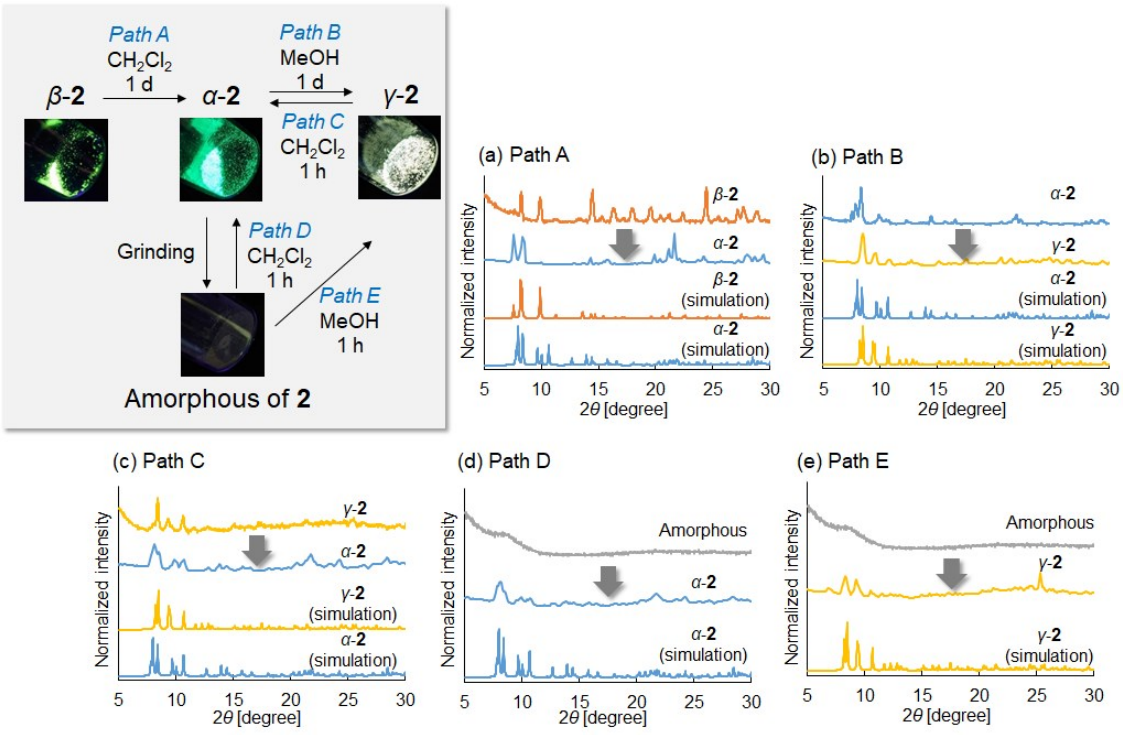

Figure S2. PXRD patterns of **2** for vapor-induced phase transitions.

7. Photophysical properties

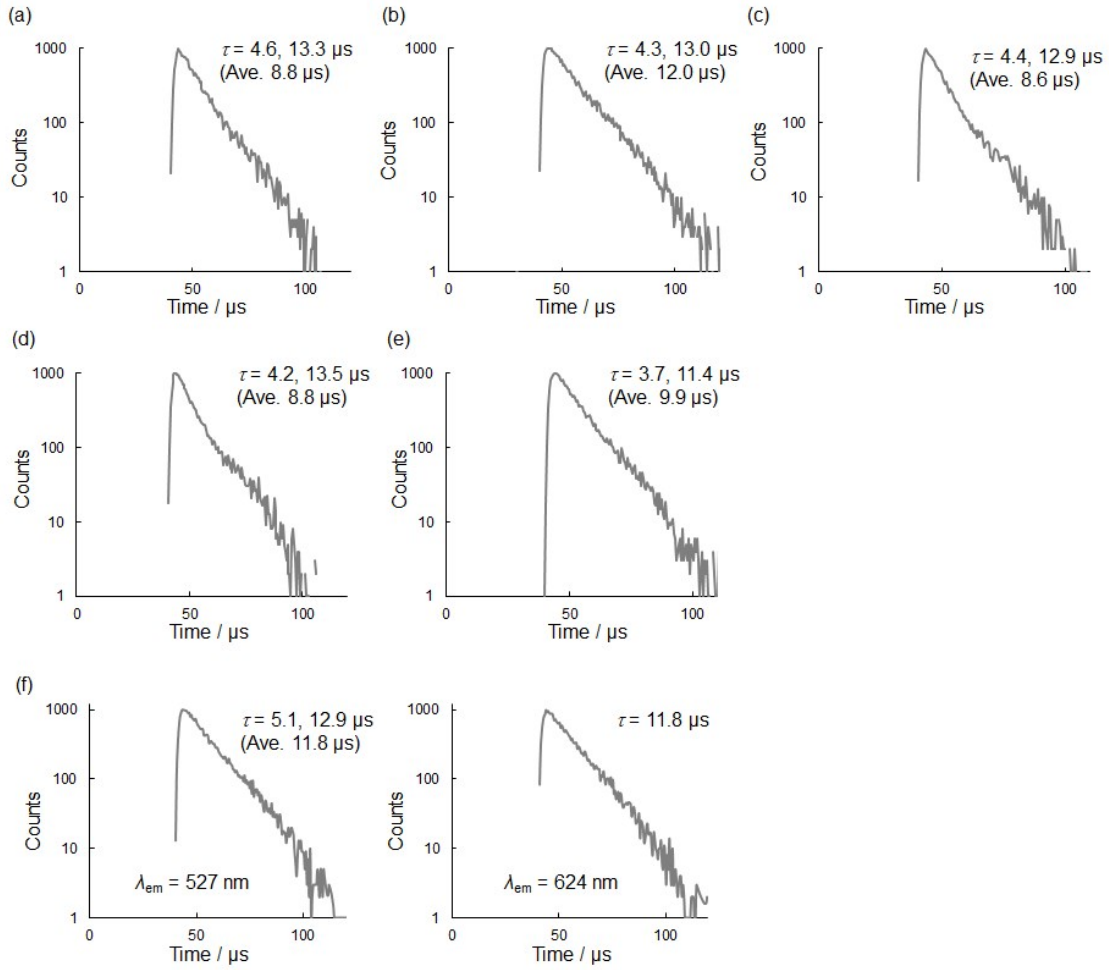

Figure S3. The emission decay kinetics of (a) α-**1** (λ_{ex} = 405 nm), (b) β-**1** (λ_{ex} = 340 nm), (c) γ-**1** (λ_{ex} = 340 nm), (d) α-**2** (λ_{ex} = 405 nm), (e) β-**2** (λ_{ex} = 340 nm), and (f) γ-**2** (λ_{ex} = 405 nm, λ_{em} = 527 nm (left) and 624 nm (right)), monitored at the emission maxima.

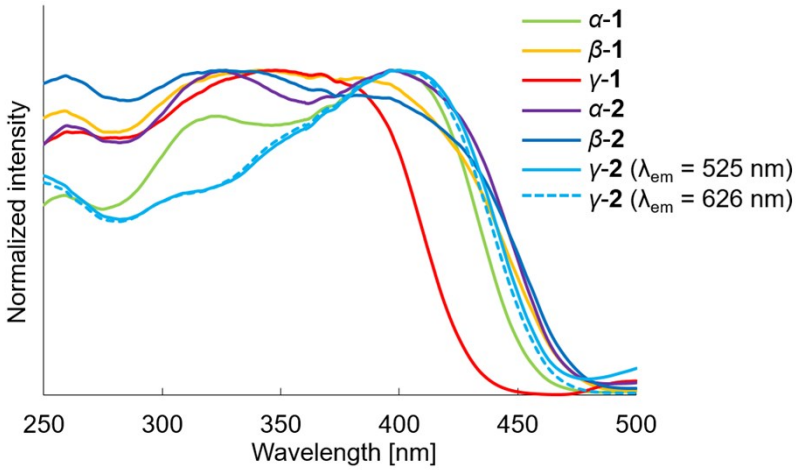

Figure S4. Excitation spectra of of **1** and **2** in the crystalline states at room temperature, monitored at the emission maxima.

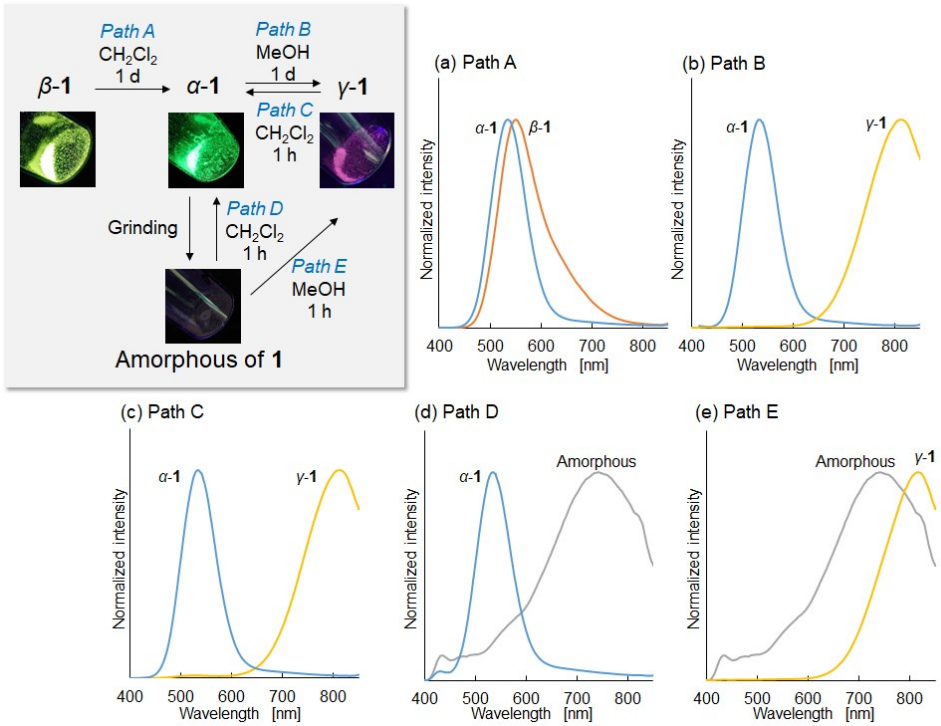

Figure S5. PL spectra of of **1** for vapor-induced phase transitions.

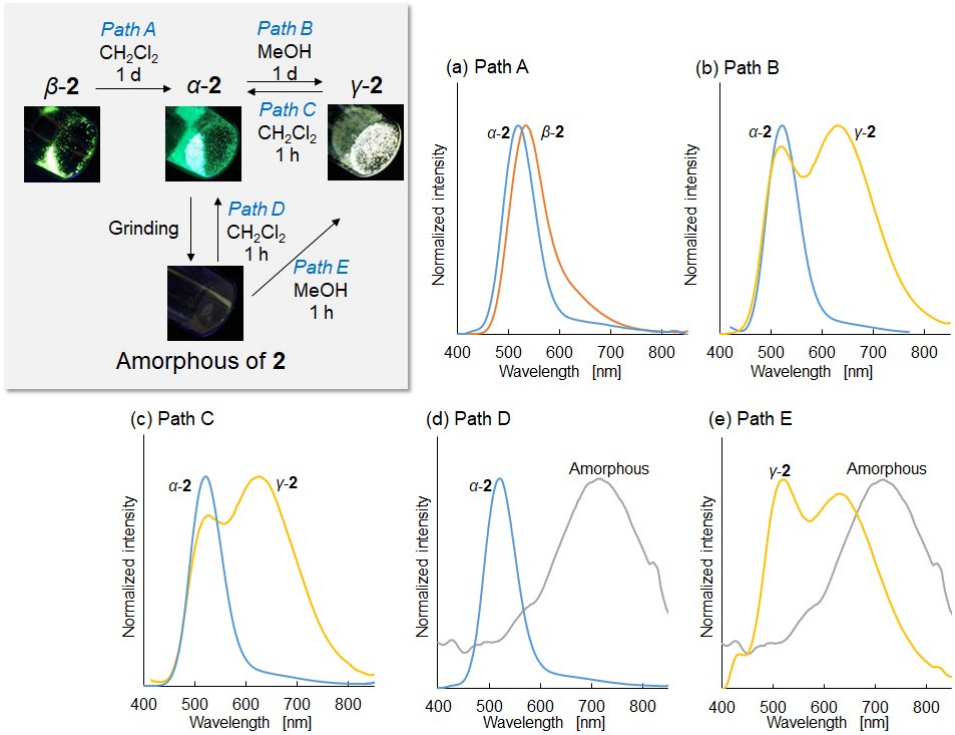

Figure S6. PL spectra of of **2** for vapor-induced phase transitions.

8. Computational investigation

To understand stability of **1** and **2**, and their electronic properties, dispersion-corrected density functional theory (DFT) calculations with B3LYP-D3 functional were employed, which are implemented in Gaussian 16 code.[10] The 6-311G** basis set was used for C, H, Cl, P, and As atoms and the SDD basis set was for Cu and Au atoms, whose core electrons were described by effective core potential (ECP). Then, we used the atomic coordination of **1** and **2** obtained from the X-ray analyses to investigate how their structures are stabilized. Average interaction energies between $[Au_2(\mathbf{L})_2]$ and a $[CuCl_2]$ moiety were obtained by using $E_{interact}$ values defined in the following equation,

$$E_{interact} = E_{total}([Au_2(\mathbf{L})_2]{-}[CuCl_2]_2) - E_{total}([Au_2(\mathbf{L})_2]) - E_{total}([CuCl_2]_2)$$

where $E_{total}([Au_2(\mathbf{L})_2]{-}[CuCl_2]_2)$ is the total energy of $[Au_2(\mathbf{L})_2]{-}[CuCl_2]_2$, as well as $E_{total}([Au_2(\mathbf{L})_2])$ and $E_{total}([CuCl_2]_2)$ are respectively the total energies of $[Au_2(\mathbf{L})_2]$ and $[CuCl_2]_2$, which are taken from $[Au_2(\mathbf{L})_2]{-}[CuCl_2]_2$). Basis set superposition errors in $E_{interact}$ values were corrected according to the literature.[11] Their $E_{interact}$ values together with key geometrical parameters are listed in Table S10.

Table S10. $E_{interact}$ values in **1** and **2** and their key geometrical parameters.

	α-**1**	*β*-**1**	*γ*-**1**	*α*-**2**	*β*-**2**	*γ*-**2-1**	*γ*-**2-2**
$E_{interact}$ [kcal/mol]	−128.7	−127.5	−131.1	−127.9	−127.0	−128.0	−119.7
Au···Cu [Å]	2.749	2.787	2.861	2.771	2.812	2.847	4.741
Au···Cl [Å]	3.433	3.305	3.369	3.476	3.336	3.311	3.232

Negative $E_{interact}$ values indicate that attractive interactions operate between $[Au_2(\mathbf{L})_2]$ and a $[CuCl_2]$ moiety to stabilize their structures. **1** and **2**, except for γ-**2-2** have Au···Cu couplings around 2.8 Å, at the same time they are stabilized by the attractive interactions $[Au_2(\mathbf{L})_2]$ and a $[CuCl_2]$ moiety. Therefore, they exhibit hetero-metallophilicity. In contrast, γ-**2-2** does not have such Au···Cu couplings, whose separations are 4.7 Å, and thus it does not exhibit hetero-metallophilicity, although γ-**2-2** is stabilized in a degree comparable to the other conformers.

The presence or absence of the hetero-metallophilicity plays an essential role in determining electronic properties in the frontier orbital region of **1** and **2**, as shown in Figure S7. Figure S7 shows orbital energies in the frontier orbital regions of **1** and **2**. In addition, we see from Figure S7 frontier orbitals whose amplitudes are on $[Au_2(\mathbf{L})_2]$ by

using red color. A first inspection of Figure S7 indicates that frontier occupied orbitals coming from the $[Au_2(\mathbf{L})_2]$ moiety cannot be seen in γ-**2**-**2** without hetero-metallophilicity. Their frontier occupied orbitals have orbital amplitudes on $[CuCl_2]_2$, although the LUMO has amplitudes on the $[Au_2(\mathbf{L})_2]$ moiety. When we look at the HOMO and LUMO of **1** and **2** except for γ-**2**-**2**, where hetero-metallophilicity appears, there are frontier occupied and unoccupied orbitals whose amplitudes are on the $[Au_2(\mathbf{L})_2]$ moiety. As an example of the $[Au_2(\mathbf{L})_2]$-based frontier orbitals, the HOMO and LUMO in α-**1** are given in Figure S8. The HOMO is generated by out-of-phase combination of 5d(Au)···5d(Au) in a σ fashion, whereas the LUMO is generated by in-phase combination of 6p(Au)···6p(Au) in a σ fashion. Because of the ~3.0 Å coupling between two Au cations, bound by methylene-linked bidentate ligands, their Au-based orbital can overlap, which is the origin of the homo-metallophilicity in $[Au_2(\mathbf{L})_2]$. A closer look at the HOMO indicates there are out-of-phase interactions between Au(I) and Cu(I) cations. Thus, the out-of-phase interactions between Au(I) and Cu(I) cations, indicating the hetero-metallophilicity, are important for appearing $[Au_2(\mathbf{L})_2]$-based occupied orbitals in the frontier orbital regions, indicating the homo-metallophilicity. In other word, the hetero-metallophilicity in**1** and **2** except for *γ*-**2**-**2** is responsible to exhibit their homo-metallophilicity.

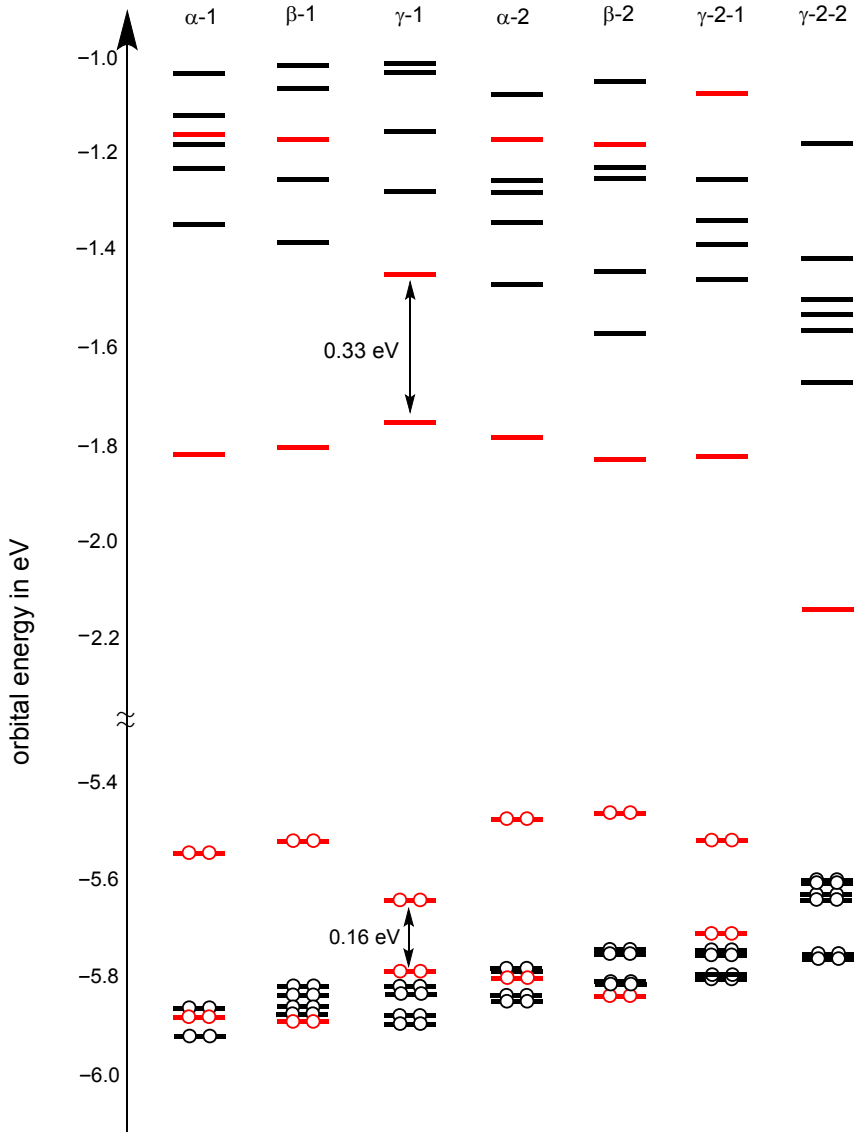

Figure S7. Orbital energies in **1** and **2** in the frontier orbital regions. Red indicates frontier orbitals whose amplitudes are mainly on the $[Au_2(\mathbf{L})_2]$.

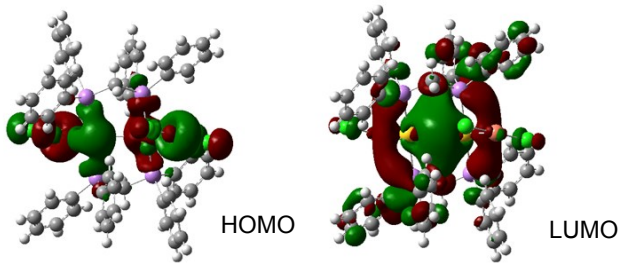

Figure S8. The HOMO and LUMO in α-**1** as an example of $[Au_2(\mathbf{L})_2]$-based frontier orbitals in **1** and **2** except for γ-**2**-**2**. Similar frontier orbitals can be seen in **1** and **2** except for γ-**2**-**2**.

Combination between Au-based frontier occupied and unoccupied orbitals is responsible for the electronic transition being the first step for the photo-emission, according to time-dependent (TD) DFT calculations. In fact, TD-DFT calculations found significant oscillator strength (*f*) in the transition from the HOMO to LUMO in **1** and **2** except for γ-**2**-**2**, as listed in Table S11. On the other hand, γ-**2**-**2** does not have any electronic transition with substantial *f* values, due to lacking frontier Au-based occupied orbitals. More interestingly, TD-DFT calculations can differentiate γ-**1** that exhibits infrared-emission from the other conformers, because Table S11 shows another electronic transition with a substantial *f* value, in addition of the HOMO-LUMO transition. In fact, γ-**1** has a *f* value in the transition from HOMO-1 to LUMO+1, being comparable to that in the HOMO-LUMO transition. In the HOMO-1, 5d(Au) and 5d(Au) overlap in out-of-phase π-type combination, whereas in the LUMO+1 6p(Au) and 6p(Au) overlap in in-phase π-type combination, as shown in Figure S9. Note that the HOMO and HOMO-1 in γ-**1** are close in energy, and the LUMO and LUMO+1 are also close. Energetically-close HOMO and HOMO-1 as well as energetically-close LUMO and LUMO+1 are characteristic in γ-**1** with the smallest Cu···Au···Au angles, which cannot be found in the other conformers with larger Cu···Au···Au angles. Thus, their energetically-close frontier orbitals would be important to exhibit infrared-emission in γ-**1**, which cannot be found in the other conformers.

Table S11. Electronic transitions, whose excitation energy (E_x) and oscillator strength *f*. Electronic transitions with *f* values larger than 0.05, obtained from time-dependent DFT calculations are listed.

α-**1**	HO→LU (E_x = 394.0 nm, *f* = 0.157)
β-**1**	HO→LU (E_x = 391.7 nm, *f* = 0.181)
γ-**1**	HO→LU (E_x = 379.5 nm, *f* = 0.078), HO-1→LU+1 (E_x = 321.2 nm, *f* = 0.060)
α-**2**	HO→LU (E_x = 398.0 nm, *f* = 0.130)
β-**2**	HO→LU (E_x = 398.9 nm, *f* = 0.150)
γ-**2**-**1**	HO→LU (E_x = 399.1 nm, *f* = 0.112)
γ-**2**-**2**	–

1) HO, LU, HO-1, and LU+1 in a structure are the HOMO, LUMO, next HOMO (HOMO-1), and next LUMO (LUMO+1), respectively. A certain electronic transition is given by the orbital labels and a laterally-facing arrow.

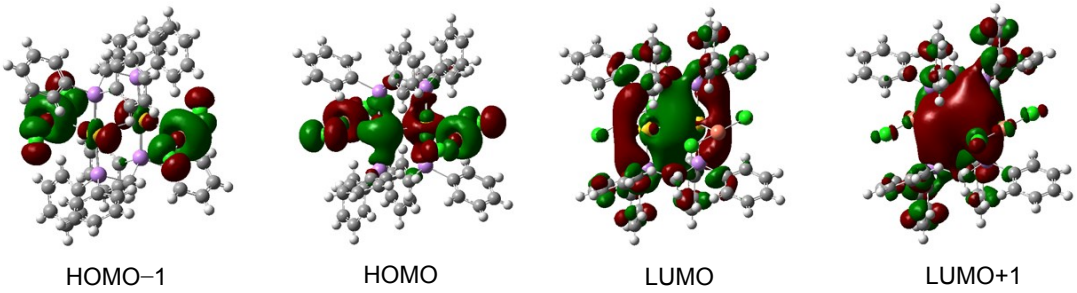

Figure S9. The next HOMO (HOMO−1), HOMO, LUMO, and next LUMO (LUMO+1) in γ-**1**, which are responsible for the electronic transitions according to time-dependent DFT calculations.

9. References

[1] H. Imoto, M. Konishi, S. Nishiyama, H. Sasaki, S. Tanaka, T. Yumura, K. Naka, *Chem. Lett.* **2019**, *48*, 1266.

[2] Uwe Monkowius, Manfred Zabel, Hartmut Yersin, *Acta Cryst.* **2009**, *E65*, m281.

[3] Marie-Claude Brandys, Michael C. Jennings, Richard J. Puddephatt, *J. Chem. Soc., Dalton Trans.* **2000**, 4601.

[4] *Fluorescence Measurements, Application to Bioscience, Measurement Method, Series 3*; Spectroscopical Society of Japan, Academic Publication Center.

[5] *CrysAlisPro*: Data Collection and Processing Software, Rigaku Oxford Diffraction, 2020, Tokyo 196-8666, Japan.

[6] Analytical numeric absorption correction using a multifaceted crystal model. R. C. Clark and J. S. Reid, *Acta Cryst.* 1995*,* **A51,** 887-897.

[7] *SHELXT*: G. M. Sheldrick, *Acta Cryst*., 2015, **C71**, 3-8.

[8] *Olex2*: O. V. Dolomanov, L. J. Bourhis, R. J. Gildea, J. A. K. Howard, H. Puschmann, *J. Appl. Cryst.* **2009**, *42*, 339.

[9] *SHELXL2016*: G. M. Sheldrick, *Acta Cryst.Sect. C Sturct. Chem.,* 2015, **C71**, 3.

[10] Gaussian 16, Revision C.01, M. J. Frisch, G. W. Trucks, H. B. Schlegel, G. E. Scuseria, M. A. Robb, J. R. Cheeseman, G. Scalmani, V. Barone, G. A. Petersson, H. Nakatsuji, X. Li, M. Caricato, A. V. Marenich, J. Bloino, B. G. Janesko, R. Gomperts, B. Mennucci, H. P. Hratchian, J. V. Ortiz, A. F. Izmaylov, J. L. Sonnenberg, D. Williams-Young, F. Ding, F. Lipparini, F. Egidi, J. Goings, B. Peng, A. Petrone, T. Henderson, D. Ranasinghe, V. G. Zakrzewski, J. Gao, N. Rega, G. Zheng, W. Liang, M. Hada, M. Ehara, K. Toyota, R. Fukuda, J. Hasegawa, M. Ishida, T. Nakajima, Y. Honda, O. Kitao, H. Nakai, T. Vreven, K. Throssell, J. A. Montgomery, Jr., J. E. Peralta, F. Ogliaro, M. J. Bearpark, J. J. Heyd, E. N. Brothers, K. N. Kudin, V. N. Staroverov, T. A. Keith, R. Kobayashi, J. Normand, K. Raghavachari, A. P. Rendell, J. C. Burant, S. S. Iyengar, J. Tomasi, M. Cossi, J. M. Millam, M. Klene, C. Adamo, R. Cammi, J. W. Ochterski, R. L. Martin, K. Morokuma, O. Farkas, J. B. Foresman, and D. J. Fox, Gaussian, Inc., Wallingford CT, 2016.

[11] S. F. Boys, F. Bernardi, *Mol. Phys.* **1970**, *19*, 553.